Contents lists available at ScienceDirect

Chemical Engineering Research and Design

journal homepage: www.elsevier.com/locate/cherd

# Numerical study of the effect of the inlet gas distributor on the bubble distribution in a bubbling fluidized bed

*Xuelian Xing*[a,b], *Chao Zhang*[c], *Bin Jiang*[b], *Yongli Sun*[b], *Luhong Zhang*[b,*], *Cedric Briens*[a,*]

[a] *ICFAR, Western University, London, ON N6A 3K7, Canada*
[b] *School of Chemical Engineering and Technology, Tianjin University, Tianjin, 300072, PR China*
[c] *Department of Mechanical and Materials Engineering, Western University, London, ON N6A 3K7, Canada*

ARTICLE INFO

*Article history:*
Received 29 July 2021
Received in revised form 30 September 2021
Accepted 17 October 2021
Available online 23 October 2021

*Keywords:*
Bubbling fluidized bed
Eulerian–Eulerian method
Inlet gas distributor
Gas distributor inclined angle
Gas bubble flux
Commercial operating conditions

ABSTRACT

Gas bubble distribution is considered one of the most critical factors affecting the Industrial Fluid Coking™ process since it influences the formation of wet agglomerates that causes fouling in the stripper section. A multi-phase Eulerian–Eulerian two-fluid method (TFM) coupled with the kinetic theory of the granular flow (KTGF) was used to investigate the hydrodynamics of a bubbling fluidized bed; the goal is to increase the flow of gas bubbles into the first half of the jet cavity formed when liquid is sprayed into the fluidized bed, thus reducing the formation of wet agglomerates. The numerical simulations under different superficial gas velocities, different gas distributor geometries, and different gas distributor inclined angles were carried out. The results showed that the predicted bubble distributions at the injection level under the lab and commercial operating conditions are similar although the particles and gases are different under those two operating conditions. More gas bubbles can be directed to the first half of the jet cavity by either increasing the gas superficial velocity (directing around 20% more gas to the specified area) or using the proposed new gas distributor (directing around 30% more gas to the specified area). The effect of the inlet gas distributor configuration on the bubble distribution is much more substantial when the inclined angle of the gas distributor is large.



## 1. Introduction

Gas–solid fluidized bed reactors have been widely applied in the petroleum oil upgrading processes, owing to their inherent benefits, such as high heat and mass transfer rates and better mixing of solids (Kunii and Levenspiel, 2013). Fluid Coking™, with its variant Flexicoking™, is one of the most commonly used processes in the refining industry to upgrade heavy crude oil or bitumen to lighter products (Yang et al., 2016). Fluid Cokers process about 1 Mbbl/day worldwide (Huc, 2010). In the Fluid Coking™ process, thermally cracking happened on the surface of the hot particles in the fluidized bed (Yang et al., 2016). However, agglomeration occurs when the liquid is not dispersed uniformly on individual particles but reaches a specific concentration to act as a binder for several solid particles. Undesired agglomerates decrease heat and mass transfer rates, thereby causing operating problems (House et al., 2004; Morales, 2013; Montes, 2014; Shi et al., 2018; Sun et al., 2020). Therefore, the rapid bypassing of wet agglomerates from the spray regions to the bottom of the reactor should be minimized (Cochet et al., 2020; Sanchez Careaga et al., 2018). As in granulation processes, intense solids mixing helps evacuate wet solids quickly from spray regions and minimize wet agglomerates formation (Eder et al., 2020). In addition, the distribution of the bubbles over the cross-section of the fluidized bed plays a vital role in agglomeration (Mohagheghi et al., 2013; Li et al., 2020a,b). Therefore, it is essential to develop methods to modify the local gas–solid hydrodynamics in the spray region and increase the solid mixing to minimize the agglomeration.

* *Corresponding authors.*
E-mail addresses: zhanglvh@tju.edu.cn (L. Zhang), cbriens@uwo.ca (C. Briens).
https://doi.org/10.1016/j.cherd.2021.10.021

**Nomenclature**

*Symbols*

| | |
|---|---|
| $\alpha_g$ | Volume fraction of gas phase |
| $\alpha_s$ | Volume fraction of solid phase |
| $\rho_g$ | Gas density, kg m$^{-3}$ |
| $\rho_s$ | Solid density, kg m$^{-3}$ |
| $\vec{\vartheta}_g$ | Gas velocity, m s$^{-1}$ |
| $\vec{\vartheta}_s$ | Solid velocity, m s$^{-1}$ |
| $\varepsilon_s$ | Gas volume fraction |
| $\varepsilon_g$ | Gas volume fraction |
| $K_{gs}$ | Gas–solid momentum exchange coefficient |
| P | Pressure, Pa |
| $p_s$ | Particulate phase pressure, Pa |
| t | Flow time, s |
| $U_{mf}$ | Minimum fluidization velocity |
| $U_t$ | Particle terminal velocity |
| $\mu$ | Shear viscosity |
| $\Theta_s$ | Granular temperature, m$^2$ s$^{-2}$ |
| $\varphi$ | Specularity coefficient |

Different methods can be applied to improve the fluidization performance. One of the methods is to improve the design of the inlet gas distributor. The primary function of the inlet distributor is to produce uniform and stable gas bubbles over the entire bed cross-section, prevent uneven fluidization, minimize bed materials erosion and decrease the leakage of solids into the plenum under the grid.

Many different distributors have been tested, and their effect on the bed hydrodynamics has been studied and represented by different parameters (Shukrie et al., 2016). Most studies have focused on a more even and uniform inlet gas distribution in the fluidized bed reactor to avoided dead or de-fluidized zones. Sánchez-Delgado et al. (2019) compared the four perforated plates with the same opening area, the different number of holes, and the results showed that as the number of holes increased, the bubble generated tends to spread more evenly. Peng et al. (2011) arranged two different gas jets: (1) center-sparse side-dense air jets arrangement; (2) center-dense side-sparse air jets and found out that the center-sparse side-dense air jets arrangement can improve the uniform of the radial flow and can significantly flat core-annulus structure. Zhou et al. (2021) discovered that the two-size-orifice distributor with 4 mm inner orifices and 2 mm outer orifices could improve the fluidization quality compared with other distributors and further promote the density segregation process of coal particles in the bed.

The difficulty of distributing gas evenly into the fluidized bed has encouraged innovation in the distributor design. Some researchers used a rotary air distributor to improve the bubble distribution and solid mixing in the bubbling fluidized bed (Sobrino et al., 2008, 2009). Brink et al. (2011) investigated the influence of the novel multi-vortex distributor on the interphase mass transfer, gas axial dispersion, and bubble size, and chemical reaction is included in the whole simulation. Using the new multi-vortex distributor dramatically improved the conversion efficiency, and a giant bubble was detected in the novel multi-vortex distributor. Inclined inlet gas distributors have also been widely used to facilitate the discharge of bed particles. Cai et al. (2015) investigated the influence of an inclined inlet gas distributor on the flow structure in the fluidized bed by measuring the residence time distribution (RTD) of the large object with four different inlet gas distributor angles and found out that increasing the angle enhanced the heterogeneity of the transverse flow in the bottom zone of the fluidized bed. Yudin et al. (2016) applied a novel inclined slotted swirling distributor to fluidized beds with different bed aspect ratios. Forty-five inclined slots triggered the early transition from fixed to fluidized bed and enhanced the solids circulation rate. However, the installation method and operation cost are always an issue with the novel design of the distributor. Since fluidized bed has many applications, not all the process needs an evenly gas distribution. The design of the distributor needs to satisfy the requirement of the process. In the Fluid Coking™ process, Li et al. (2020a,b) found that modifying the gas lateral or radial distribution at the spray level can significantly improve the liquid distribution, which will be further studied in this paper.

Another issue that has been neglected is that it is essentially impossible to conduct experiments under the same conditions and on the same scale as in commercial processes. For example, Fluid Cokers operate at a temperature of about 550 °C, at a pressure of 200–300 kPa, and with a circulating flowrate of hot coke particles around 100 ton/min. Furthermore, the fluidized bed is filled with hot coke particles, and the hydrocarbon is steam-atomized and injected horizontally into the bed through multiple nozzles. Song et al. (2008) investigated the hydrodynamics of a fluidized bed reactor, a scaled-down commercial unit. Both FCC particles and fluid coke particles were used under the same conditions, and similar voidage distribution and solids momentum flux distribution were observed. However, in their study, the difference in the particle properties between FCC ($\rho_p = 1700\,kg/m^3$, $\overline{d_p} = 99\,\mu m$) and fluid coke ($\rho_p = 1600\,kg/m^3$, $\overline{d_p} = 133\,\mu m$) are not obvious, which could be one of the reasons for the similar results. Qi et al. (2008) used sand particles and FCC as fluidized material to study the combined effect of particle properties and nozzle gas distributor design in two risers. They found that the radial distribution in the fully developed section is more uniform with sand particles, and the axial distribution is more uniform in FCC particles. However, there is no further study or explanation for this phenomenon.

CFD has been used to study the hydrodynamics of the bubbling fluidized beds with different gas distributor designs. The Eulerian–Lagrange and the Eulerian–Eulerian are the two approaches commonly used to predict the impact of the distributor on the performance of fluidized beds. The Eulerian–Eulerian approach uses the two-fluid model (TFM) and is typically applied in the fluidized beds where the concentration of the solid particles is relatively high. Peng et al. (2011) investigated the flow multiplicity phenomenon in a 2-D CFB riser numerically using the Eulerian–Eulerian approach with k–$\varepsilon$ turbulence model for each phase. Five different inlet gas distributors (fully opened, right-opened, left-opened, center-opened, and 3-jets) were employed to study the solid concentration profiles and velocities at different heights in the bed. It was found that the fully developed flow profiles depended on the inlet flow profile. Zhou et al. (2021) simulated the gas–solid two-phase flow in the fluidized bed by Euler dual-fluid model with nine different gas distributor structures; apart from the pressure drop analysis, they also checked the distributor effect on the density-segregation process of coal particles. Raza et al. (2021) investigated the mixing pattern and pressure drop using TFM of finite volume method-based solver ANSYS FLUENT with three diverse distributor plate designs: perforated plate, 90° slotted plate, and 45° swirling slotted plate. Venier et al. (2019) applied both the CFD codes ANSYS Fluent® v19.2 and OpenFOAM® v6.0 to test the performance of their Eulerian–Eulerian method implementations on several fluidization operating conditions when using Geldart A, B, and D and when using two different fluidized bed geometries: a three-dimensional lab-scale system and a pseudo-two-dimensional setup. Moreover, the results showed that both codes give accurate predictions of the fluidization patterns for standard conditions (i.e., Geldart B on a cylindrical arrangement). In the CFD-DEM method, the trajectory of each particle is tracked based on the Newton's second law, which makes the CFD-DEM approach more computationally expensive than the TFM approach.

This study developed an accurate numerical model to simulate the gas–solid two-phase flows in bubbling fluidized beds. To the best of our knowledge, no previous work combined the inclined distributor and the different gas distributor configurations to concentrate gas bubbles in a particular area in the fluidized bed. First, the proposed numerical model was validated by comparing the numerical results with the experimental data obtained in a laboratory-scale bubbling fluidized bed from Li et al. (2020a,b). Then, this verified numerical method was used first to study the possibility of using different particles and gases in the lab condition to predict the bubble distribution in the commercial condition.


**Fig. 1 – Layout of the paper.**

The layout of this research is presented in Fig. 1. Section 1 includes the introduction of the topic, literature review, and the motivation of this research. Section 2 will introduce the configuration of the fluidized bed. In the third section, all the computational models, related equations, and procedures will be presented. Then, in Section 4, the discussion and case study will involve the numerical model validation, the effect of gas and particle properties, and different gas inlet distributors. Finally, Section 5 will provide the conclusions with further directions.

## 2. Configurations of the experimental bubbling fluidized bed

The experimental data from a lab-scale bubbling fluidized bed reactor with a rectangular cross-data obtained by Li et al. (2020a) were used to validate the numerical model. The experimental setup is shown in Fig. 2(a). The height of the fluidized bed unit is 2.28 m, with an expansion in the upper section, and the bed thickness is 0.1 m. Other geometrical parameters are shown in Fig. 2(a).

As shown in Fig. 2(b), three different inlet gas distributors were considered to investigate the effect of the inlet gas distributor on bubble distributions in the fluidized bed. The base case is the Even inlet gas distributor in which the ten active gas tuyeres are evenly distributed. The second one is the Western inlet gas distributor with ten active tuyeres near the left-hand side of the column, and the third one is the Eastern inlet gas distributor with ten active tuyeres near the right-hand side.

The local volumetric flux of the bubble gas can be obtained from the triboelectric signal generated by the impact of the gas bubbles on each probe (Portoghese et al., 2007). The lateral profile of the bubble gas flux was reported with the ratio of the local bubble flux to the average cross-sectional volumetric flux. The total gas flux is equal to the local gas voidage multiplied by the local gas velocity, which includes the gas flux in the emulsion phase and the gas flux in the bubble phase. The solids are Geldart's group B particles, and their minimum fluidization velocity is 0.033 m/s. Over the range of superficial gas velocities explored in this paper, the bubble phase flux is at least 91.75% of the total gas flux. Therefore, the local gas bubble flux was assumed to be the same as the total local gas flux.

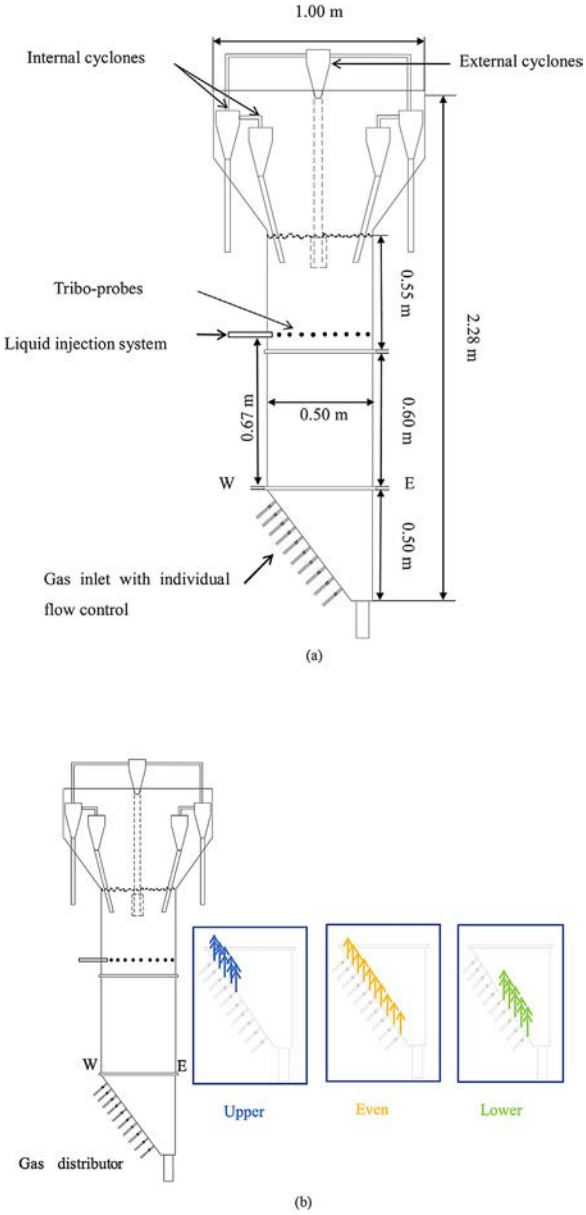


**Fig. 2 – Configuration of the lab-scale bubbling fluidized bed (Li et al., 2020a) (a) overall experimental system (b) different inlet gas distributors.**

The profile of the gas bubble flux is calculated by:

$$q_{bi}/\overline{q_b} \tag{1}$$

where
$q_{bi}$ is the local gas bubble flux
$\overline{q_b}$ is the average cross-sectional gas bubble flux

$$q_{bi} \approx \varepsilon_i \cdot \vartheta_i \tag{2}$$

where
$\varepsilon_i$ is the local gas voidage
$\vartheta_i$ is the local gas velocity

$$\overline{q_b} = \frac{1}{x_w} \cdot \int_0^{x_w} q_{bi} \cdot dx \tag{3}$$

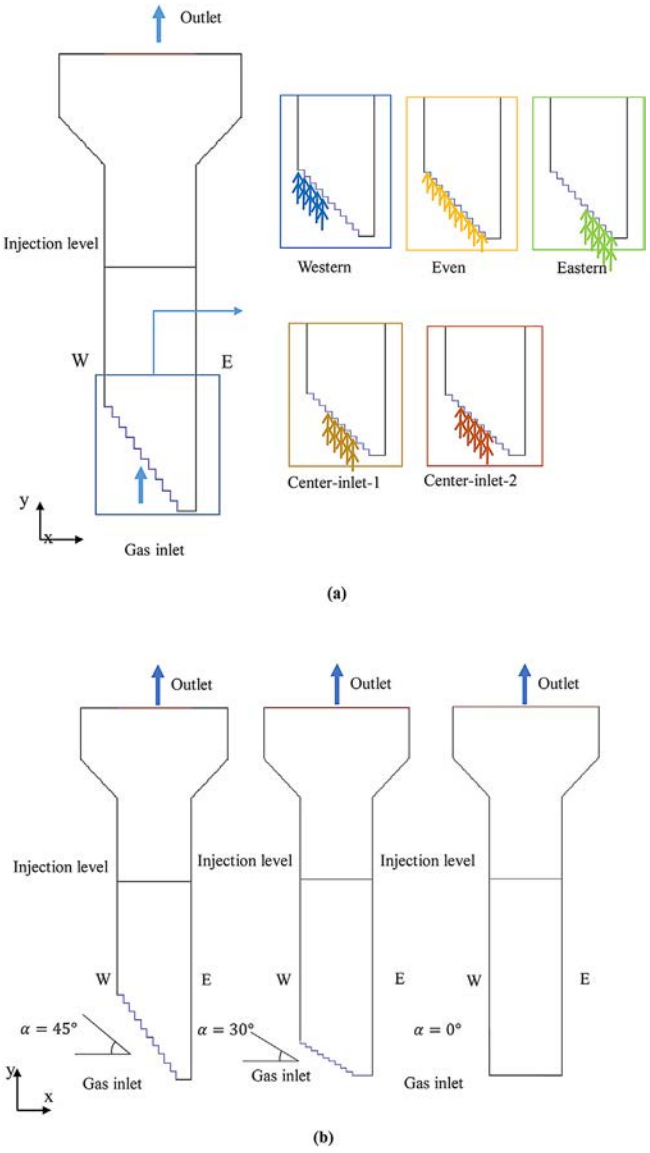


**Fig. 3 – Different geometries used in the simulations (a) different inlet gas distributors (b) different gas inlet distributor angles.**

## 3. Numerical simulation modelling

In this study, the commercial CFD package ANSYS Fluent 18.2 was used to perform the numerical simulation to obtain the hydrodynamics of bubbling fluidized bed over a wide range of fluidization velocities using different inlet gas distributor configurations. Both the gas and particle phases are treated as a continuum, whereas the particle properties, particle-particle interaction, and particle-gas interaction need to be defined explicitly. Currently, the kinetic theory of granular flow (KTGF) is widely applied to close the governing equations for the solid phase (Lu et al., 2015; Lun and Savage, 1986). In the previous study (Xing, 2020, pp. 56–60), the predicted gas volume fraction distributions in the bubbling fluidized bed using the laminar and turbulent models were compared with the experimental data. It was found that the results from the laminar model were closer to the experimental data since the gas flow velocity in a bubbling bed is low. Therefore, the laminar model is applied in this work. A two-dimensional fluidized bed, shown in Fig. 3(a), was applied in the simulation. Fig. 3(b) shows the three different inlet gas distributors with an angle with a horizontal plane of 45°, 30°, or 0°. In the experimental setup, a 45° angle inlet gas distributor was used. If not specified, the results are based on the experimental setup.

### 3.1. Governing equations

The Eulerian–Eulerian approach is applied to simulate the flow in a gas–solid fluidized bed. Gas and solid phases could be present simultaneously in the same computational volume. Therefore the volume fraction for each phase is introduced (ANSYS Inc., 2016). The continuity equations for gas (g) and solid (s) phases can be written as:

$$\frac{\partial}{\partial t}\left(\alpha_g \rho_g\right) + \nabla\left(\alpha_g \rho_g \vec{\vartheta}_g\right) = 0, \tag{4}$$

$$\frac{\partial}{\partial t}\left(\alpha_s \rho_s\right) + \nabla\left(\alpha_s \rho_s \vec{\vartheta}_s\right) = 0, \tag{5}$$

$$\alpha_s + \alpha_g = 1 \tag{6}$$

where $\alpha$ is the volume fraction, $\rho$ is the density and $\vec{\vartheta}$ is the velocity vector

The momentum equation for the gas phase is the Navier–Stokes's equation:

$$\frac{\partial}{\partial t}\left(\alpha_g \rho_g \vec{\vartheta}_g\right) + \nabla\left(\alpha_g \rho_g \vec{\vartheta}_g \vec{\vartheta}_g\right) = -\alpha_g \nabla p + \nabla \cdot \bar{\bar{\tau}}_g + \alpha_g \rho_g g + K_{gs}\left(\vec{\vartheta}_s - \vec{\vartheta}_g\right), \tag{7}$$

where $p$ is the hydrodynamic pressure, $K_{gs}$ is the momentum exchange coefficient between gas and solid phases.

Other constitutive equations for the two-phase flows based on the kinetic theory of granular flow are listed in Appendix A. Gidaspow and Symlal-O'Brien models were developed for both dilute and dense regions in the fluidized beds, and they are the most commonly used models in two-phase flow simulations. We compared the results from those two drag force models and found that the predictions from the Symlal-O'Brien model are closer to the experimental results.The drag model considers the interactions between the gas and solid phases during the fluidization process. The momentum exchange coefficient between the phases, $K_{gs}$, is determined based on the Syamlal and O'Brien drag model (Syamlal et al., 1993).

The Syamlal and O'Brien drag model is based on the single-particle terminal velocity and adjusted based on the fluid properties and the expected minimum fluidization velocity.

$$K_{gs} = \frac{3\alpha_s \alpha_g \rho_g}{4 v_{r,s}^2 d_s} C_D\left(\frac{Re_s}{v_{r,s}}\right)\left|\vec{v}_s - \vec{v}_g\right|, \tag{8}$$

$$v_{r,s} = 0.5\left(A - 0.06Re_s + \sqrt{(0.06Re_s)^2 + 0.12Re_s(2B - A) + A^2}\right), \tag{9}$$

$$A = \alpha_g^{4.14},$$

$$B = c1 \cdot \alpha_g^{1.28} \text{ for} \alpha_g \le 0.85,$$

$$B = \alpha_g^{d1} \text{ for } \alpha_g > 0.85$$

**Table 1 – Grid size-independent test.**

| Name | Mesh interval spacing (mm) | Grid nodes | Grid cells | Bed pressure drop (Pa) | Difference (%) |
|---|---|---|---|---|---|
| Mesh-1 | 2 × 2 | 226,854 | 225,458 | 7920 | – |
| Mesh-2 | 5 × 2 | 102,983 | 102,221 | 7945 | 0.31 |
| Mesh-3 | 5 × 4 | 54,808 | 54,171 | 8025 | 1.00 |

where $d1 = 1.28 + \frac{\log_{10}C1}{\log_{10}0.85}$

$$C_D = \left(0.63 + \frac{4.8}{\sqrt{\left(Re_s/v_{r,s}\right)}}\right)$$

$$Re_s = \frac{\rho_g d_s \left|\vec{v}_s - \vec{v}_g\right|}{\mu_g},$$

where $C_D$ is the drag coefficient, and $Re_s$ is the Reynolds number

### 3.2. *Boundary conditions*

Rather than using a uniform inlet boundary condition, which was implemented widely in other fluidized bed simulations, the gas inlet boundary condition was specified based on the nozzle diameters and locations used in the experiments. Two rows of 10 tuyeres were used in the experimental column to supply gas over the whole column depth. For this 2D simulation, a single row of the gas inlet represented each couple of side-by-side tuyeres in the third direction. The gas was injected into the bed through the tuyeres nozzles in the verti-

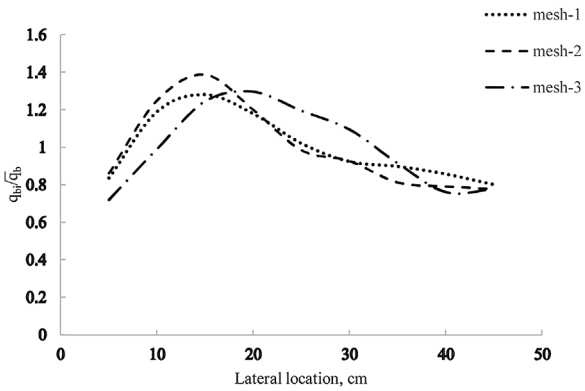


**Fig. 4 – Lateral gas bubble distribution profiles at the injection level with different grid sizes under the superficial gas velocity of 0.4 m/s.**

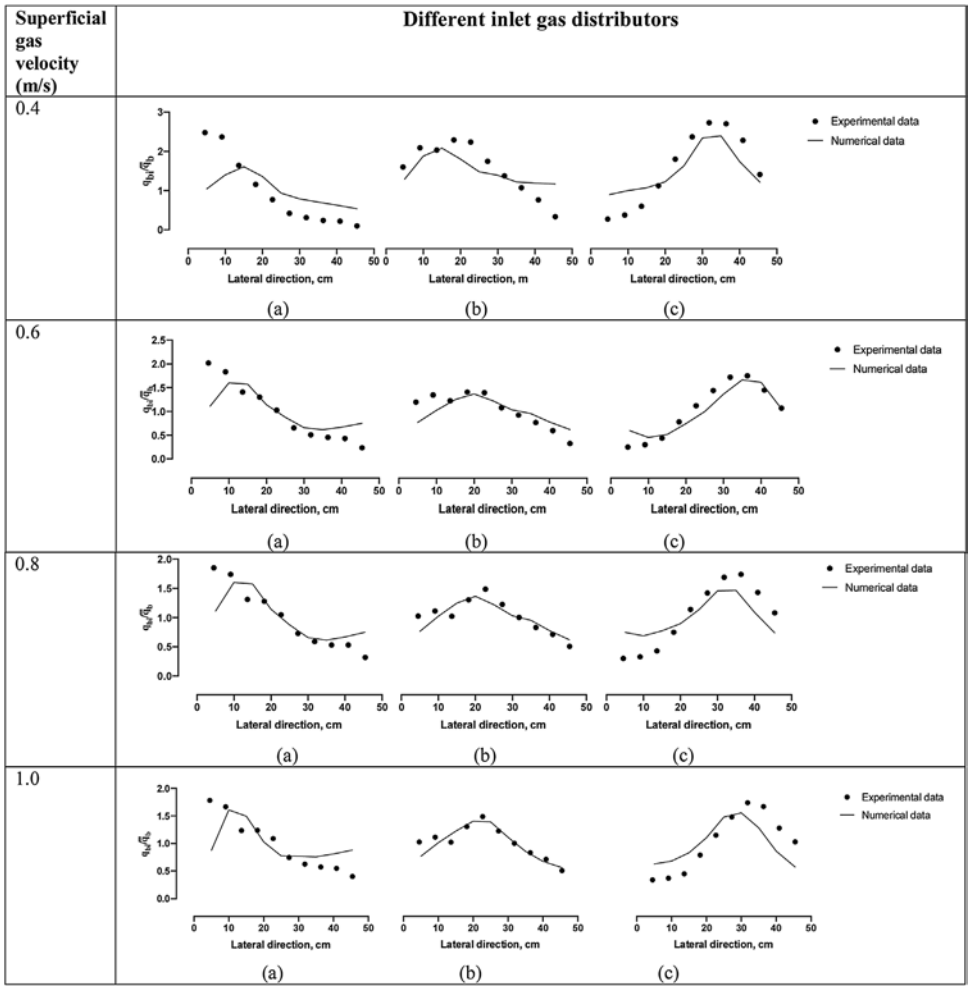


**Fig. 5 – Comparison of the numerical and experimental results (Li et al., 2020a) for the radial gas bubble distributions at the injection level of the bubbling fluidized bed (a) Western inlet gas distributor, (b) even inlet gas distributor, (c) Eastern inlet gas distributor.**

cal direction, as shown in Fig. 2. In the Even inlet distributor case, all ten inlets are open to inject gas. However, only five inlets near the left-hand side of the fluidized bed reactor are open for the Western inlet distributor case. In the Eastern inlet distributor case, five inlets near the right-hand side are open. To obtain the same superficial velocity in the freeboard, the gas flow rate through each inlet in the eastern and western cases was double the gas flowrate through each inlet in the even case, i.e., the total flow rates for all three cases are the same. Simulations were also performed for two additional inlet gas distributor configurations for which no experimental data were available to determine whether such inlet gas distributors would be more effective. In every single inlet, the uniform gas velocity condition was used, and the pressure outlet was applied for exiting. The inlet gas velocity was specified based on the gas flowrate and nozzle diameters used in the experiment. The atmosphere pressure was selected at the outlet boundary condition for the reactor. No-slip boundary condition for the gas phase and Johnson and Jackson's (Johnson and Jackson, 1987) slip boundary condition for the solid phase were used.

$$\vec{U}_{S,W} = -\frac{6\mu_s\alpha_{s,max}}{\sqrt{3}\pi\rho_s\phi\alpha_s g_{0,ss}\sqrt{\Theta_s}}\frac{\partial\vec{U}_{S,W}}{\partial n}, \quad (10)$$

The specularity coefficient $\varphi$ is an empirical parameter that represents the particle-wall collision. The value of the specularity coefficient depends on the wall roughness. $\varphi = 0$ means a perfect specular collision, and $\varphi = 1$ means a perfect diffusion collision. Moreover, the value of 0.0001 is chosen based on an earlier study (Hong et al., 2012).

### 3.3. Solution procedure

The phase-coupled SIMPLE algorithm was applied for the pressure-velocity coupling to solve the mass and momentum conservation equations. The quadratic upwind interpolation for convection kinematics (QUICK) scheme was used to discretize the convection terms in the momentum equations. Finally, the modified type of the high-resolution interface capturing (HRIC) scheme was used to obtain the gas or solid phase volume fraction.

The physical properties of gas and particles are specified in Appendix B. It was assumed that particles are of uniform size, and their diameter equals the Sauter mean diameter. A time step of 0.001 s with 100 maximum iterations per time step was chosen, and a convergence criterion of $1 \times 10^{-5}$ for continuity equation and $5 \times 10^{-4}$ for other scaled residual components was specified. The simulations were run for 30 s, and the time-averaged values were obtained using the data from the last 20 s since a steady condition was achieved after 10 s.

### 3.4. Grid size-independent test

In the CFD simulation, it is necessary to ensure that the grid size is appropriate. Therefore, a grid size sensitivity test was performed using three grid resolutions. The mesh intervals were $2 \times 2$, $5 \times 2$, and $5 \times 4$ mm, respectively. The grid convergence index (GCI) based on the average gas bubble flux was calculated for three grids; the results showed that the grid sizes used in this work are in the asymptotic range of convergence. All the simulations for the grid-independent tests were carried out at the same superficial gas velocity 0.4 m/s for the Even inlet gas distributor case. Table 1 shows the pressure drops predicted across the bed using three different mesh sizes. It can be seen that the percentage difference between mesh-2 and mesh-1, which is 0.31%, is less than that between mesh-2 and mesh-3, which is 1.00%. Therefore, mesh 2 is used for the rest of the simulations. The time-averaged gas bubble flux profiles in the injection level for different grid sizes are shown in Fig. 4. Based on the comparison, it can be seen that the difference in the results between mesh-1 and mesh-2 is small enough. Therefore, mesh-2, the medium-sized mesh (102,221 cells), was used in this study.

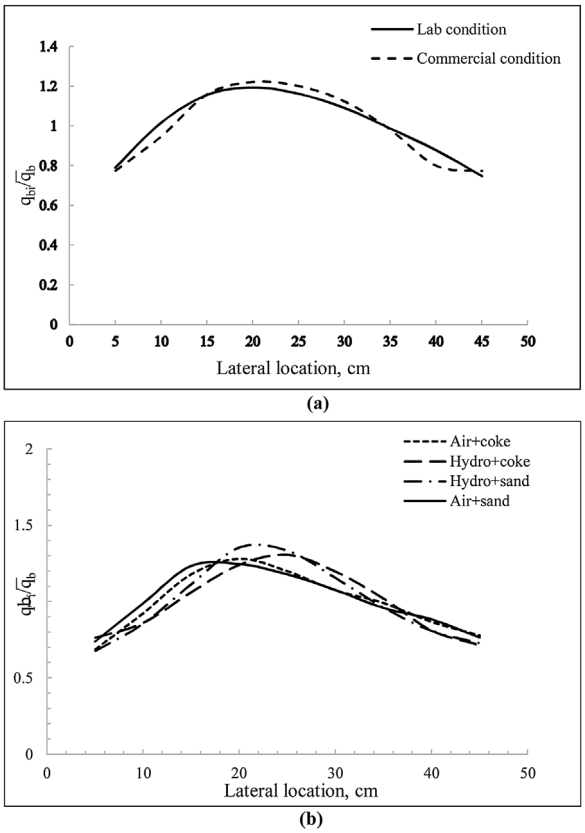


**Fig. 6 – Comparison of lateral gas bubble distributions under the superficial gas velocity of 0.60 m/s at H = 1.00 m (a) air + sand and hydro + coke cases (b) of air + sand and hydro + coke, air + coke, and hydro + coke cases.**

## 4. Results and discussion

### 4.1. CFD model validation

The radial bubble distribution has been proven to have a significant impact on the injected liquid distribution, which affects the performance of the bubbling fluidized bed. Therefore, it was measured in the experimental work using the E-probe (Li et al., 2020b) and is used to validate the numerical results. Fig. 5 shows the numerical results of the gas flux profiles on the injection level compared with experimental results for three different inlet gas distributor configurations under different superficial gas velocities. For the Even inlet gas distributor configuration, both the predicted and measured profiles indicate a moderate lateral variation in the gas bubble flux, but the flux is lower on the right-hand side, which the inclined inlet gas distributor likely causes. The predicted results are in good agreement with the experimental data at higher superficial gas velocities (0.8 m/s and 1.0 m/s). In the Eastern inlet gas distributor case, the predicted and measured profiles show

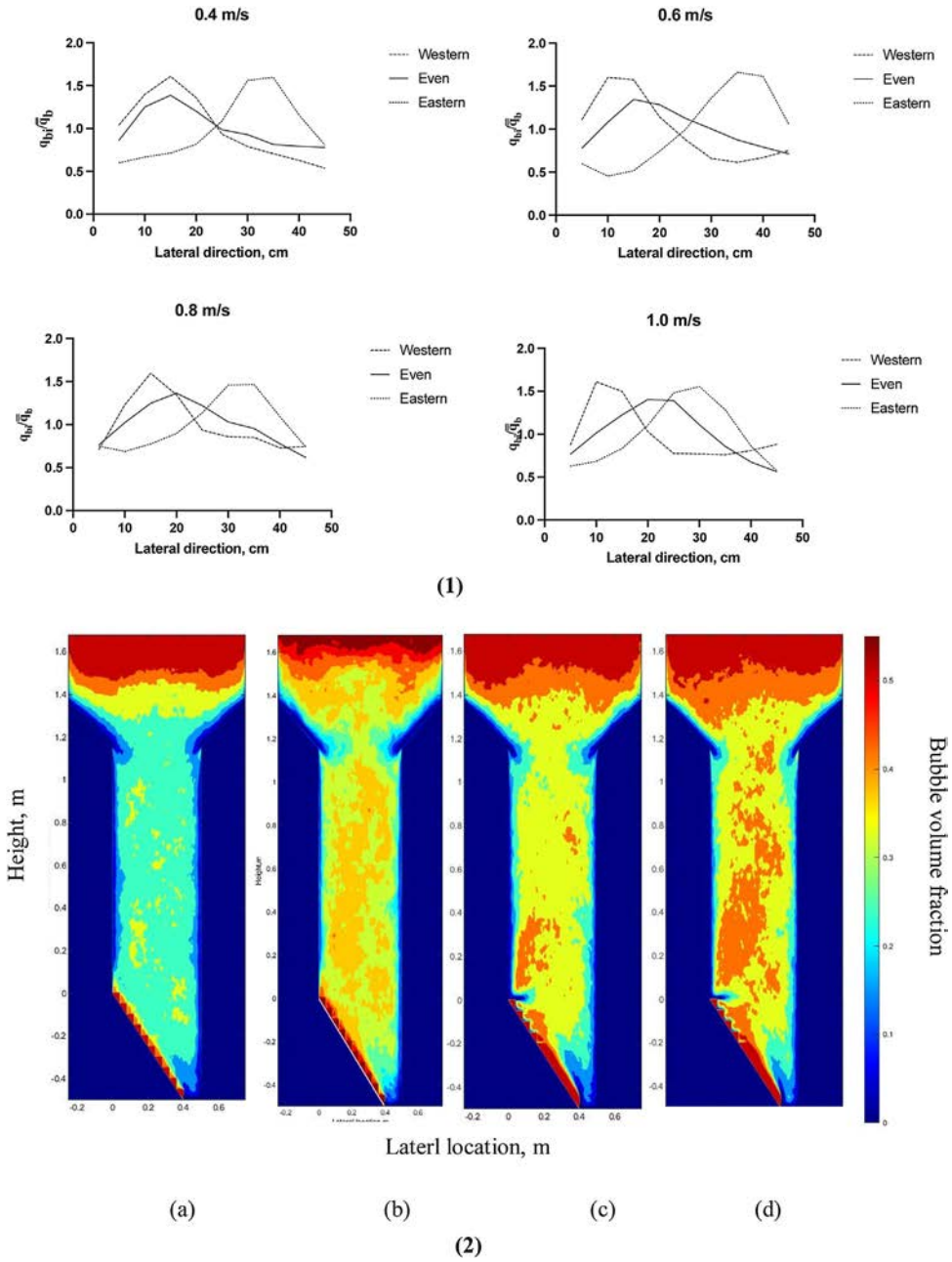


**Fig. 7 – Different inlet gas distributors under different superficial gas velocities (a) $u_g$ = 0.4 m/s, (b) $u_g$ = 0.6 m/s, (c) $u_g$ = 0.8 m/s, (d) $u_g$ = 1.0 m/s (1) time-averaged lateral gas bubble distribution at the "injection level" (2) time-averaged bubble volume flux contours.**

that the gas bubbles are concentrated on the right-hand side, and both the predicted and measured bubble fluxes peak at around 35 cm in the lateral direction. In the Western gas inlet distributor configuration, the predicted and measured profiles show that the gas bubbles are concentrated on the left-hand side, and both predicted and measured bubble fluxes peak at around 10 cm in the lateral direction. Quantitative discrepancies are noticed between the predicted and measured results for the two points near the left-hand side of the wall, which might result from either the boundary conditions used in numerical simulation or the wall effect on the triboelectric probe during experiments since the probe near the wall is around 5 cm away from the wall, and most of the differences happened nearer the wall. The boundary conditions for the solid phase are based on empirical correlations, which depend on the solid particle properties and wall conditions, and they will affect the predictions near the wall. In all cases, the predicted bubble flux variation is slightly smaller than that from the experimental data. However, the general gas bubble distribution tendency is consistent with the experimental observation.

### 4.2. *Effect of the gas and particle properties*

In commercial units, like thermal crackers or fluid cokers, the fluidized bed is filled with hot coke particles, and the hydrocarbon is steam-atomized and injected horizontally into the bed through multiple nozzles. However, there is a debate about whether the experimental study should use the particles from the actual high-temperature full-scale process or more controllable and measurable particles. Therefore, fluidization simulations were carried out in the lab-scale setup

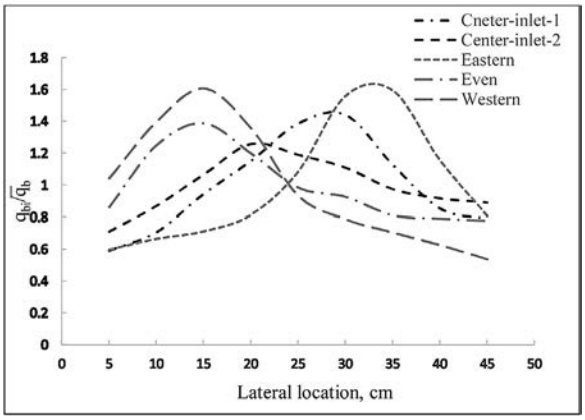


**Fig. 8 – Gas bubble profiles at the injection level with different inlet gas distributor configurations under the superficial gas velocity of 0.4 m/s.**

with dry compressed air and silica sand in this work. This study aims to determine whether the predicted hydrodynamic behaviours obtained using different particles and gases, which are representative of the lab and commercial conditions, are similar.

The gas and particle properties under these two conditions, the lab condition (dry compressed air and silica sand) and the commercial condition (vaporized hydrocarbons and steam and coke particles). The results under these two conditions are shown in Fig. 6(a). The comparison is based on the gas bubble profiles at the injection level under the same superficial gas velocity of 0.60 m/s. It can be seen that the gas bubble distribution profiles under the two different conditions are similar.

In addition to the lab and commercial conditions, two more conditions, dry compressed air + coke particles and vaporized hydrocarbons + silica sand, are also used to investigate the effect of the gas and particle properties on the performance of the bubbling bed reactors. The comparison of the lateral gas bubble distributions under the four conditions is present in Fig. 6(b). In general, the gas bubble flux profiles under the four different conditions at H = 1.0 m are similar. However, the differences between the cases with identical solid particles but different gases are more significant than that between the cases with the same gas and different solid particles, i.e., the gas bubble profiles for the cases of air with sand and coke particles have a similar flux profile, the same for the cases of the vaporized hydrocarbons and steam with sand and coke particles. Therefore, the gas properties influence the gas bubble distributions more than the particle properties. In general, the gas bubble flux distribution profiles are similar for the lab and commercial conditions.

### 4.3. *Effect of the inlet gas distributor on the bubble distribution*

Fig. 7 (1) shows that even at the injection level, well above the inlet gas distributor, the gas inlet condition due to the configuration of the inlet gas distributor strongly affects the lateral gas bubble distribution. This is observed at the inlet superficial gas velocities ranging from 0.4 m/s to 1.0 m/s. To compare the lateral profiles of the bubble flux using those three inlet gas distributors under different inlet superficial gas velocities, it is easy to observe that both the Eastern and Western inlet gas distributors give a higher peak bubble flux than that from the Even inlet gas distributor. This is because the peak bubble fluxes from all three inlet gas distributors are off-center. Furthermore, the gas velocity did not substantially change the relative gas bubble profile on the injection level. However, an increase in the superficial gas velocity by 0.2 m/s resulted in redirecting 10% more gas bubble flux to the first half of the jet cavity, which, according to the experimental results (Li et al., 2020b), can reduce agglomerate formation.

Moreover, the Eastern gas distributor with 1 m/s gas velocity is the best choice compared to others. Fig. 7 (2) shows the averaged gas volume fraction contours using the Western inlet gas distributor configuration under different gas superficial velocities (0.4 m/s–1.0 m/s). Clearly, as the superficial gas velocity increases, more gas flows into the fluidized bed, and the freeboard increases. Moreover, the low gas voidage region exists for all four different superficial gas velocities but gets smaller as the superficial gas velocity increases. However, the fluidization is more stable when the velocity is relatively low, so it is better to modify the condition in Eastern gas velocity, in which 0.4 m/s is chosen in the following study. Therefore, two additional gas inlet distributor configurations are proposed: the Center-inlet -1 and Center-inlet-2, as shown in Fig. 2(a). Fig. 8 shows that using the two new inlet gas distributor configurations, the peak in gas bubble flux at the injection level is being moved from the left to the right of the column and any position in-between. Therefore, modifying the inlet gas distributor configuration could move the gas bubble flux peak at the injection level to a desired lateral position. If considering the gas concentrate into the first half of the jet cavity, the Center-inlet -1 is the best as it has concentrated at least 30% more gas bubble flux into the required area than the Even inlet gas distributor.

Fig. 9 (1) confirms that the influence of the inlet gas distributor configurations on the bubble distribution persisted over the entire bed height based on the time-averaged gas volume fraction contours from the five different gas distributor configurations. Bubbles are concentrated on the west side for the case using the Western inlet gas distributor (Fig. 9 (1) (a)), are relatively evenly distributed for the case using the Even inlet gas distributor (Fig. 9 (1) (b)) and are concentrated in the central part for the case of the Eastern inlet gas distributor (Fig. 9 (1) (c)). The difference between the two center inlet gas distributors (Fig. 9 (1) (d) and (e)) is slight in the lower part of the fluidized bed reactor. There are more bubbles located on the lower side around the injection level (0.6 m–0.8 m) for the Center-inlet-1case than the Center-inlet-2 case, which has a more uniform gas bubble profile on the injection level, as shown in Fig. 9 (1) ((d) and (e)).

Fig. 9 (2) shows the time-average velocity contours using the five different inlet gas distributors at a superficial gas velocity of 0.4 m/s. Compared to the case of the Even inlet gas distributor (Fig. 9 (2) (b)), the uneven inlet gas distributors promote the formation of zones of high gas velocities above the inlet gas distributor. Generally, these high-velocity zones become attenuated at higher locations, but with some inlet gas distributors, they propagate to relatively higher locations, as shown in Fig. 9 (2) ((e) and (f)).

As discussed above, increasing the gas velocity can improve gas bubble performance by concentrating more bubbles to the expected zone. In the lower gas velocity zone, modifying the inlet gas distributor configuration, the gas bubble flux peak at the injection level could be moved to a desired lateral position. Moreover, Center-inlet-1 works better than others to concentrate bubble flow to the first half of the jet cavity.

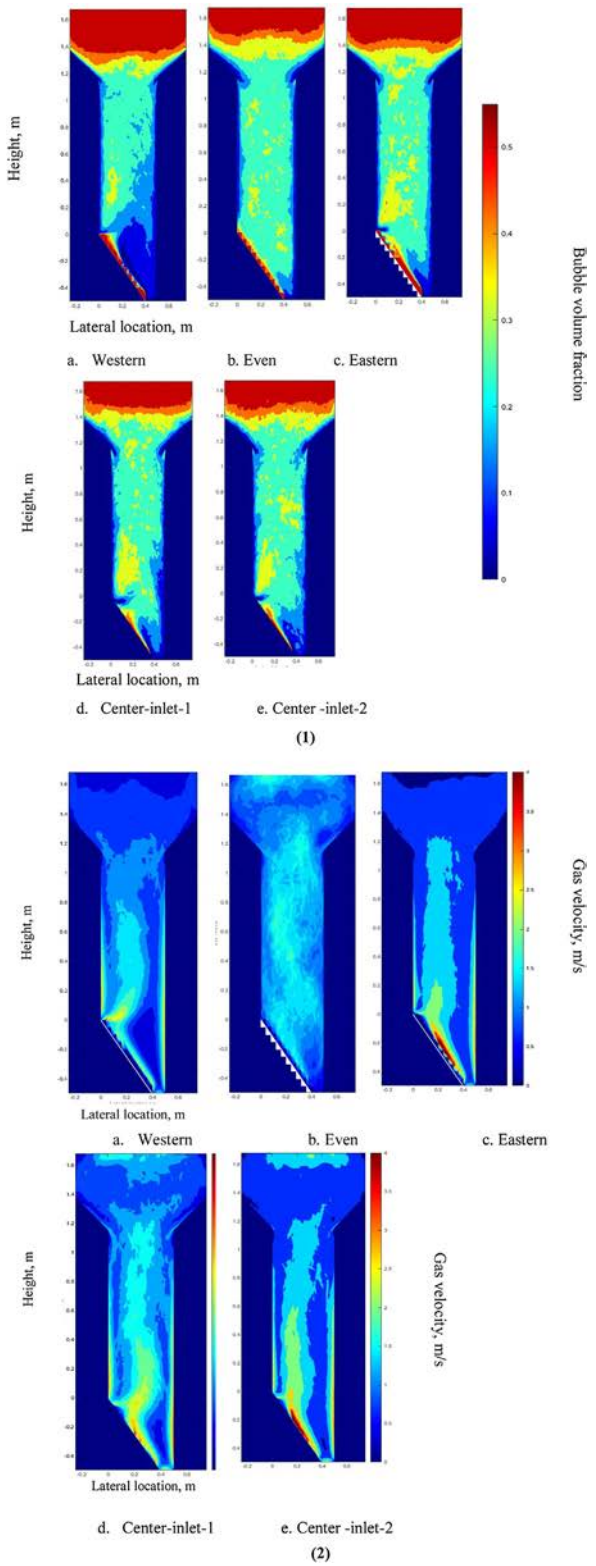


**Fig. 9 – Different inlet gas distributors under the superficial gas velocity of 0.4 m/s (1) time-averaged bubble volume flux contours (2) time-averaged gas velocity contours.**

### 4.4. *Effect of the inclined angle of the inlet gas distributor*

Fig. 10 presents the influence of the inclined angle of the air inlet gas distributor on the gas bubble flux profile on the injection level, with Even gas inlet distribution. Increasing the inclined angle resulted in moving the peak value location from the center (25 cm) to the left-hand side (around 14 cm). A possible reason is that as the inclined angle increases, tangential airflow through the inlet gas distributor increases, increasing the bubbles transversal mixing and weakening the concentration of gas bubbles in the center of the reactor.

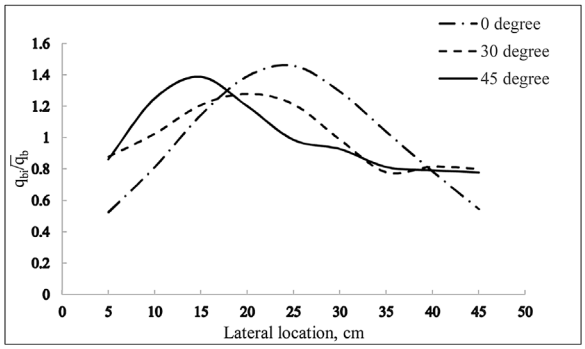


**Fig. 10 – Comparison of different inlet gas distributor inclined angles using the even inlet gas distributor configuration under the superficial gas velocity of 0.4 m/s.**

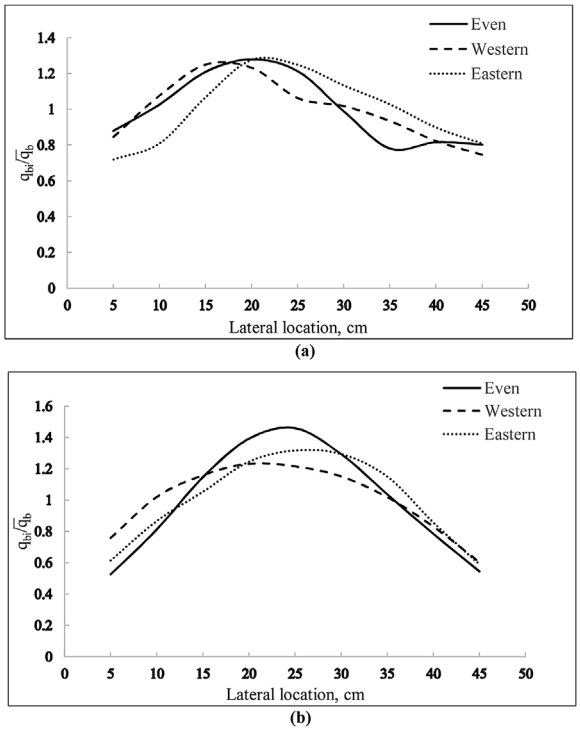


**Fig. 11 – Comparison of the lateral gas bubble distributions at the injection level using three different inlet gas distributor configurations under the superficial velocity of 0.4 m/s (a) the distributor angle of 30° (b) the flat distributor.**

When combining the effects of the inlet gas distributor configuration and the inclined inlet gas distributor angle, Fig. 11 shows that for the flat inlet and 30° inclined inlet gas distributors, the effect of inlet gas distributor configuration is much weaker when compared to the 45° inclined distributor (Fig. 7 (1) (a)). If the objective is to adjust the gas bubble distribution at the injection level by modifying the inlet gas distributor configuration, an inlet gas distributor with a substantial incline is preferable. However, if only considering concentrated bubble flow in the specified area, the Eastern inlet gas distributor is better than the other two for both inclined inlet gas distributors. The flat inlet gas distributor is always better than the inclined inlet gas distributor regardless of the different inlet gas distributor configurations.

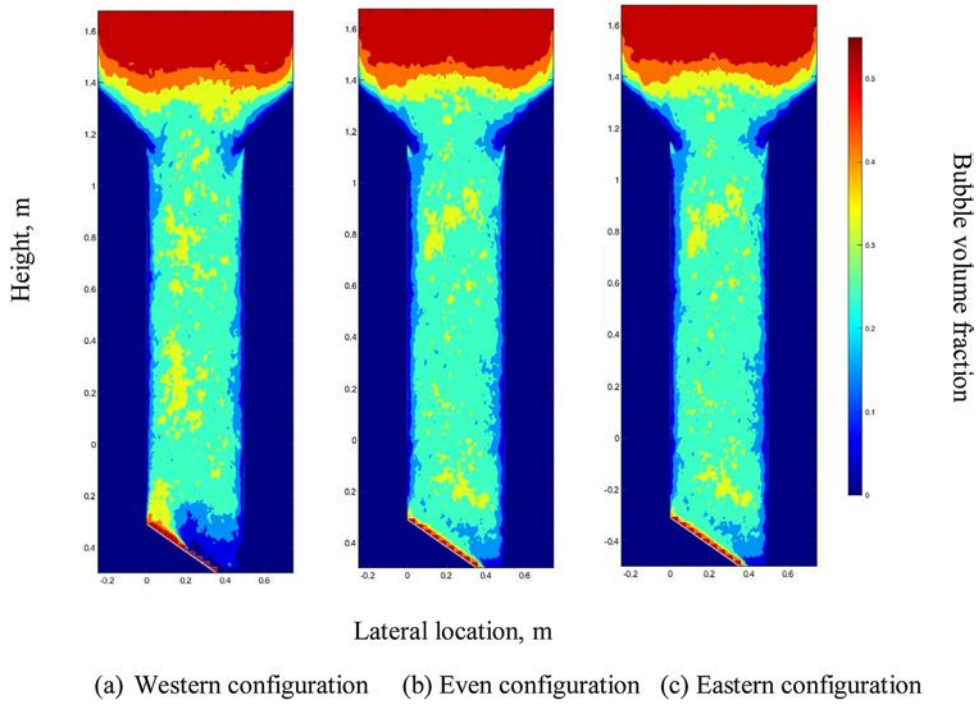


**Fig. 12 – Time-averaged bubble volume flux contours using three different inlet gas distributor configurations with 30°distributor inclined angle under the superficial gas velocity of 0.4 m/s.**

Fig. 12 shows the time-averaged gas volume fraction contours using three inlet gas distributors with a 30° inclined. It can be seen that the inlet gas distributor configuration affects the bubble distribution in the entire bed, but more on the bottom region of the bed. More gas bubbles are on the left-hand side when using the Western inlet gas distributor, and more gas bubbles are concentrated close to the right-hand side when using the Eastern inlet gas distributor. In the case of the Even inlet gas distributor, bubbles are evenly distributed in the entire fluidized bed. The contours for the 30° inlet gas distributor are similar to the contours of the 45° distributor, as shown in Fig. 9 (1) ((a)–(c)).

The results show that the flat inlet gas distributor has the optimum angle for concentrating bubble flow to the first half of the jet cavity. However, for the inclined gas inlet distributor, the Eastern gas inlet distributor is better than other configurations on concentrating bubbles. The different inlet gas distributor works more effectively to change the gas bubble distribution at the injection level when it has a substantial incline.

## 5. Conclusions

A multi-phase Eulerian–Eulerian two-fluid method (TFM) coupled with the kinetic theory of granular flow (KTGF) can successfully predict the impact of the inlet gas distribution on the lateral profile of the gas bubble flux at a level well above the inlet gas distributor level.

The gas bubble distributions on the injection level were similar enough so that the gas and particle in lab conditions can be used for studying the fluid coking process.

Increasing the superficial gas velocity can significantly improve the gas bubble distribution. Around 20% more gas can be directed to the specified area (the first half of the jet cavity) with an increase in the superficial gas velocity from 0.4 m/s to1.0 m/s for all three different inlet gas distributors.

Gas bubble distributions in a bubbling fluidized bed can be modified by changing the configuration of the inlet gas distributor. The inlet gas distributor configuration can significantly affect the gas bubble lateral distribution well above the distributor level. By applying the Center-inlet-1inlet gas distributor, more than 30% gas can be directed to the specified area (the first half of the jet cavity) than the Even inlet gas distributor, so the agglomerates can be reduced.

Gas bubble distributions in a bubbling fluidized bed can also be modified by changing the inlet gas distributor angle. However, the effect of the inlet gas distributor is much more substantial for distributors with a significant inclined angle. Therefore, if the objective is to adjust the gas bubble distribution at the injection level by modifying the inlet gas distributor configuration, an inlet gas distributor with a significant inclined angle is preferable.

## Funding information

Funding was received from China Scholarship Council (Grant # 201500090111).

## Conflict of interest

The authors declare that they have no known competing financial interests or personal relationships that could have appeared to influence the work reported in this paper.

## Declaration of Competing Interest

The authors report no declarations of interest.

## Acknowledgments

The authors would like to acknowledge financial support from the China Scholarship Council and the NSERC-Syncrude Industrial Research Chair in Fluid Coking Technologies. The authors would also like to thank Yuan Li for supplying the experimental data used in this study.

## Appendix A

Constitutive equations of kinetic theory of granular flow

Granular temperature transport equation:

$$\frac{3}{2}\left[\frac{\partial}{\partial t}\left(\rho_s\alpha_s\Theta_s\right)+\nabla\cdot\left(\rho_s\alpha_s\vec{\vartheta}_s\Theta_s\right)\right]=\left(-p_s\bar{\bar{I}}+\bar{\bar{\tau}}_s\right):\nabla\vec{\vartheta}_s+\nabla\cdot\left(k_{\Theta_s}\nabla\Theta_s\right)-\gamma_{\Theta_s}+\varphi_{ls} \quad (A1)$$

where

$\left(-p_s\bar{\bar{I}}+\bar{\bar{\tau}}_s\right):\nabla\vec{\vartheta}_s$ is the generation of energy by the solid stress tensor,

$k_{\Theta_s}\nabla\Theta_s$ is the diffusion of energy,

$\gamma_{\Theta_s}$ is the collisional dissipation of energy, and

$\varphi_{ls}$ is the energy exchange between the $l$th solid phase and the $s$th solid phase.

The stress tensors for gas and solid phases are:

$$\bar{\bar{\tau}}_g=\alpha_g\mu_g\left(\nabla\vec{v}_g+\nabla\vec{v}_g^{\,T}\right)-\frac{2}{3}\alpha_g\mu_g\nabla\cdot\vec{v}_g\bar{\bar{I}} \quad (A2)$$

$$\bar{\bar{\tau}}_s=\alpha_s\mu_s\left(\nabla\vec{v}_s+\nabla\vec{v}_s^{\,T}\right)+\alpha_s\left(\lambda_s-\frac{2}{3}\mu_s\right)\nabla\cdot\vec{v}_s\bar{\bar{I}} \quad (A3)$$

Correlation for the solid shear viscosity:

$$\mu_s=\mu_{s,col}+\mu_{s,kin}+\mu_{s,fr} \quad (A4)$$

Correlation for the collisional viscosity:

$$\mu_{s,col}=\frac{4}{5}\alpha_s\rho_s d_s g_{0,ss}\left(1+e_{ss}\right)\left(\frac{\Theta_s}{\pi}\right)^{1/2}\alpha_s \quad (A5)$$

Correlation for the kinetic viscosity:

$$\mu_{s,kin}=\frac{\alpha_s d_s\rho_s\sqrt{\Theta_s\pi}}{6\left(3-e_{ss}\right)}\left[1+\frac{2}{5}\left(1+e_{ss}\right)\left(3e_{ss}-1\right)\alpha_s g_{0,ss}\right] \quad (A6)$$

Correlation for the frictional viscosity:

$$\mu_{s,fr}=\frac{P_{friction}\sin\varphi}{2\sqrt{I_{2D}}} \quad (A7)$$

Correlation for the solid bulk viscosity:

$$\lambda_s=\frac{4}{3}\alpha_s^2\rho_s d_s g_{0,ss}\left(1+e_{ss}\right)\left(\frac{\Theta_s}{\pi}\right)^{1/2} \quad (A8)$$

Correlation for the solid pressure:

$$p_s=\alpha_s\rho_s\Theta_s+2\rho_s\left(1+e_{ss}\right)\alpha_s^2 g_{0,ss}\Theta_s \quad (A9)$$

Correlation for the radial distribution function:

$$g_{0,s}=\left[1-\left(\frac{\alpha_s}{\alpha_{s,max}}\right)^{\frac{1}{3}}\right]^{-1} \quad (A10)$$

Syamlal-O'Brien model for the diffusion coefficient of granular temperature:

$$k_{\Theta_s}=\frac{15d_s\rho_s\alpha_s\sqrt{\Theta_s\pi}}{4\left(41-33\eta\right)}\left[1+\frac{12}{5}\eta^2\left(4\eta-3\right)\alpha_s g_{0,ss}+\frac{16}{15\pi}\left(41-33\eta\right)\eta\alpha_s g_{0,ss}\right] \quad (A11)$$

$$\eta=\frac{1}{2}\left(1+e_{ss}\right) \quad (A12)$$

## Appendix B

Table B1 Summary of physical properties of the reactor, particles and gas (Li et al., 2020a).

| | | |
|---|---|---|
| **Reactor** | | |
| $H_0$ | Initial bed height [m] | 1.6 |
| $U_{mf}$ | Minimum fluidization velocity [m/s] | 0.027 |
| P | Operating pressure [atm] | 1 |
| T | Operating temperature [°C] | 130 |
| $\varepsilon_{s_0}$ | Initial solids packing | 0.6 |
| **Gas** | | |
| $\rho_g$ | Gas density [kg/m$^3$] | 1.177 |
| $\mu_g$ | Shear viscosity [kg/ms] | $1.85\times10^{-5}$ |
| $U_g$ | Superficial velocity [m/s] | 0.4, 0.6, 0.8, 1.0 |
| **Particles** | | |
| $\rho_s$ | Solid density [kg/m$^3$] | 2650 |
| $d_s$ | Sauter mean diameter [μm] | 190 |

Table B2 Gas and particle properties under the lab and commercial operating conditions.

| | Lab condition | Commercial condition |
|---|---|---|
| **Gas** | Dry compressed air | Vaporized hydrocarbons and steam* |
| Gas density, $\rho_g$, kg/m$^3$ | 1.177 | 2.28 |
| Gas viscosity, μ, Pa·s | $1.85\times10^{-5}$ | $2.5\times10^{-5}$ |
| **Particle** | Silica sand | Coke particles |
| Particle diameter, μm | 190 | 145 |
| Particle density, $\rho_g$, kg/m$^3$ | 2650 | 1600 |
| Geldart powder group | B | B |
| Minimum gas velocity, m/s | 0.033 | 0.009 |

*The gas and particle properties are from Glatt (2018).

Table B3 Boundary conditions.

| | |
|---|---|
| **Inlet** | |
| Gas-phase | Superficial gas velocity |
| **Wall** | |
| Gas-phase | No-slip velocity |
| Solid-phase | Partial-slip |
| | Specularity coefficient ($\varphi$): 0.0001 |
| **Outlet** | |
| Gas-phase | Pressure-outlet |
| Solids-phase | Pressure-outlet |

Table B4 Information on all the cases simulated in this study.

| Case number | Superficial gas velocity, m/s | Gas distributor angle, | Gas distributor configuration | Gas properties | Particle properties |
|---|---|---|---|---|---|
| 1 | 0.4 | 45 | Western | Dry compressed air | Silica sand |
| 2 | 0.4 | 45 | Even | Dry compressed air | Silica sand |
| 3 | 0.4 | 45 | Eastern | Dry compressed air | Silica sand |
| 4 | 0.4 | 45 | Center-inlet-1 | Dry compressed air | Silica sand |
| 5 | 0.4 | 45 | Center-inlet-2 | Dry compressed air | Silica sand |
| 6 | 0.6 | 45 | Western | Dry compressed air | Silica sand |
| 7 | 0.6 | 45 | Even | Dry compressed air | Silica sand |
| 8 | 0.6 | 45 | Eastern | Dry compressed air | Silica sand |
| 9 | 0.8 | 45 | Western | Dry compressed air | Silica sand |
| 10 | 0.8 | 45 | Even | Dry compressed air | Silica sand |
| 11 | 0.8 | 45 | Eastern | Dry compressed air | Silica sand |
| 12 | 1.0 | 45 | Western | Dry compressed air | Silica sand |
| 13 | 1.0 | 45 | Even | Dry compressed air | Silica sand |
| 14 | 1.0 | 45 | Eastern | Dry compressed air | Silica sand |
| 15 | 0.6 | 45 | Even | Vaporized hydrocarbons and steam* | Coke particles |
| 16 | 0.6 | 45 | Even | Vaporized hydrocarbons and steam* | Silica sand |
| 17 | 0.6 | 45 | Even | Dry compressed air | Coke particles |
| 18 | 0.4 | 30 | Even | Dry compressed air | Silica sand |
| 19 | 0.4 | 30 | Western | Dry compressed air | Silica sand |
| 20 | 0.4 | 30 | Eastern | Dry compressed air | Silica sand |
| 21 | 0.4 | 0 | Even | Dry compressed air | Silica sand |
| 22 | 0.4 | 0 | Western | Dry compressed air | Silica sand |
| 23 | 0.4 | 0 | Eastern | Dry compressed air | Silica sand |

*The gas and particle properties are from Glatt (2018).

## References


Ansys® Academic Research Mechanical, Release 18.2, Help System, Fluent 18.2 User Guide, ANSYS, Inc.

Brink, H.G., Saayman, J., Nicol, W., 2011. Two dimensional fluidised bed reactor: performance of a novel multi-vortex distributor. Chem. Eng. J. 175, 484–493, http://dx.doi.org/10.1016/j.cej.2011.09.077.

Cai, R., Gu, C., Zhang, Y., Li, Q., Meng, A., 2015. Effect of inclined distributor on the motion behavior of a large spherical object in the bottom zone of a fluidized bed. Powder Technol. 277, 147–155, http://dx.doi.org/10.1016/j.powtec.2015.02.058.

Cochet, Y., Briens, C., Berruti, F., McMillan, J., Sanchez Careaga, F.J., 2020. Impact of column geometry and internals on gas and particle flows in a fluidized bed with downward solids circulation: effect of lateral injection profile and baffles. Powder Technol. 372, 275–289, http://dx.doi.org/10.1016/j.powtec.2020.05.071.

Eder, C., Hofer, G., Beer, J., Pröll, T., 2020. Particle mixing in bubbling fluidized bed reactors with immersed heat exchangers and continuous particle exchange. Ind. Eng. Chem. Res. 59, 19736–19750, http://dx.doi.org/10.1021/acs.iecr.0c03568.

Glatt, E., 2018. Modeling Fluid Coker Cyclone Fouling. Western University, London, ON, Canada.

Hong, K., Wang, W., Zhou, Q., Wang, J., Li, J., 2012. An EMMS-based multi-fluid model (EFM) for heterogeneous gas-solid riser flows: Part I. Formulation of structure-dependent conservation equations. Chem. Eng. Sci. 75, 376–389, http://dx.doi.org/10.1016/j.ces.2012.03.022.

House, P.K., Saberian, M., Briens, C.L., Berruti, F., Chan, E., 2004. Injection of a liquid spray into a fluidized bed: particle-liquid mixing and impact on fluid coker yields. Ind. Eng. Chem. Res. 43, 5663–5669, http://dx.doi.org/10.1021/ie034237q.

Huc, A.-Y., 2010. Heavy Crude Oils: From Geology to Upgrading: An Overview. Editions TECHNIP, Pairs, France.

Johnson, P.C., Jackson, R., 1987. Frictional–collisional constitutive relations for granular materials, with application to plane shearing. Great Br. 176, 67–93, http://dx.doi.org/10.1017/S0022112087000570.

Kunii, D., Levenspiel, O., 2013. Fluidization Engineering. Elsevier.

Li, Y., Careaga, F.S., Briens, C., Berruti, F., McMillan, J., 2020a. Impact of local fluidized bed hydrodynamics on the distribution of liquid sprayed into the bed. Powder Technol. 367, 326–335, http://dx.doi.org/10.1016/j.powtec.2020.03.012.

Li, Y., Jahanmiri, M., Careaga, F.S., Briens, C., Berruti, F., McMillan, J., 2020b. Applications of electrostatic probes in fluidized beds. Powder Technol. 370, 64–79, http://dx.doi.org/10.1016/j.powtec.2020.05.033.

Lu, G., Third, J.R., Müller, C.R., 2015. Discrete element models for non-spherical particle systems: from theoretical developments to applications. Chem. Eng. Sci. 127, 425–465, http://dx.doi.org/10.1016/j.ces.2014.11.050.

Lun, C.K.K., Savage, S.B., 1986. The effects of an impact velocity dependent coefficient of restitution on stresses developed by sheared granular materials. Acta Mech. 63, 15–44, http://dx.doi.org/10.1007/BF01182538.

Mohagheghi, M., Hamidi, M., Berruti, F., Briens, C., McMillan, J., 2013. Study of the effect of local hydrodynamics on liquid distribution in a gas—solid fluidized bed using a capacitance method. Fuel 107, 236–245, http://dx.doi.org/10.1016/j.fuel.2013.01.059.

Montes, A., 2014. Factors Affecting Bed Agglomeration in Bubbling Fluidized Bed Biomass Boilers. MESc. Thesis. Western University, London, ON, Canada, https://ir.lib.uwo.ca/etd/2325.

Morales, C.B., 2013. Development and Application of an Experimental Model for the Fluid Coking Process. M.Sc Thesis.

Peng, B., Xu, J., Zhu, J., Zhang, C., 2011. Numerical and experimental studies on the flow multiplicity phenomenon for gas-solids two-phase flows in CFB risers. Powder Technol. 214, 177–187, http://dx.doi.org/10.1016/j.powtec.2011.07.014.

Portoghese, F., Berruti, F., Briens, C., Chan, E., 2007. Novel triboelectric method for characterizing the performance of nozzles injecting gas-atomized liquid into a fluidized bed. Chem. Eng. Process. Process Intensif. 46, 924–934, http://dx.doi.org/10.1016/j.cep.2007.05.003.

Qi, X.-B., Huang, W.-X., Zhu, J., 2008. Comparative study of flow structure in circulating fluidized bed risers with FCC and sand particles. Chem. Eng. Technol. 31, 542–553, http://dx.doi.org/10.1002/ceat.200700485.

Raza, N., Ahsan, M., Mehran, M.T., Naqvi, S.R., Ahmad, I., 2021. Computational analysis of the hydrodynamic behavior for different air distributor designs of fluidized bed gasifier. Front. Energy Res. 9, 692066, http://dx.doi.org/10.3389/fenrg.2021.692066.

Sanchez Careaga, F.J., Briens, C., Berruti, F., McMillan, J., Gray, M., 2018. Agglomerate behavior in a recirculating fluidized bed with sheds: effect of sheds. Adv. Powder Technol. 29, 1758–1770, http://dx.doi.org/10.1016/j.apt.2018.04.011.

Sánchez-Delgado, S., Marugán-Cruz, C., Serrano, D., Briongos, J.V., 2019. Distributor performance in a bubbling fluidized bed: effects of multiple gas inlet jet and bubble generation. Chem. Eng. Sci. 195, 367–380, http://dx.doi.org/10.1016/j.ces.2018.09.035.

Shi, Q., Li, S., Tian, S., Huang, Z., Yang, Yao, Liao, Z., Sun, J., Wang, J., Yang, Yongrong, 2018. Investigating agglomeration behaviors in high temperature gas–Solid fluidized beds with liquid injection. Ind. Eng. Chem. Res. 57, 5482–5494, http://dx.doi.org/10.1021/acs.iecr.8b00311.

Shukrie, A., Anuar, S., Oumer, A.N., 2016. Air distributor designs for fluidized bed combustors: a review. Eng. Technol. Appl. Sci. Res. 6, 1029–1034, http://dx.doi.org/10.48084/etasr.688.

Sobrino, C., Almendros-Ibañez, J.A., Santana, D., de Vega, M., 2008. Fluidization of Group B particles with a rotating distributor. Powder Technol. 181, 273–280, http://dx.doi.org/10.1016/j.powtec.2007.05.014.

Sobrino, C., Ellis, N., de Vega, M., 2009. Distributor effects near the bottom region of turbulent fluidized beds. Powder Technol. 189, 25–33, http://dx.doi.org/10.1016/j.powtec.2008.05.012.

Song, X., Grace, J.R., Bi, H., Lim, C.J., Chan, E., Knapper, B., McKnight, C., 2008. Experimental simulation of the reactor section of fluid cokers: comparison of FCC and fluid coke particles. Can. J. Chem. Eng. 84, 161–169, http://dx.doi.org/10.1002/cjce.5450840203.

Sun, J., Tian, S., Li, S., Yang, Yao, Huang, Z., Shi, Q., Wang, J., Yang, Yongrong, Wang, F., 2020. Experimental and modeling investigation of liquid-induced agglomeration in a gas–solid fluidized bed with liquid spray. Ind. Eng. Chem. Res. 59, 11810–11822, http://dx.doi.org/10.1021/acs.iecr.0c01130.

Syamlal, M., Rogers, W., O'Brien, T.J., 1993. MFIX Documentation Theory Guide. Technical Note.

Venier, C.M., Reyes Urrutia, A., Capossio, J.P., Baeyens, J., Mazza, G., 2019. Comparing ANSYS Fluent® and OpenFOAM® simulations of Geldart A, B and D bubbling fluidized bed hydrodynamics. HFF 30, 93–118, http://dx.doi.org/10.1108/HFF-04-2019-0298.

Xing, X., 2020. Numerical Study of the Effect of Gas Distributors and Baffles on the Bubble Distribution, Gas and Solid Mixing in a Fluidized Bed. Western University, London, ON, Canada.

Yang, N., Zhou, Y.L., Qi, T.Y., Lu, Z.Y., 2016. Bitumen cracking using liquid injection. Pet. Sci. Technol. 34, 1164–1171, http://dx.doi.org/10.1080/10916466.2016.1183026.

Yudin, A.S.M., Anuar, S., Oumer, A.N., 2016. Improvement on particulate mixing through inclined slotted swirling distributor in a fluidized bed: an experimental study. Adv. Powder Technol. 27, 2102–2111, http://dx.doi.org/10.1016/j.apt.2016.07.023.

Zhou, E., Lv, B., Deng, X., Qin, X., Fang, C., 2021. Hydrodynamic and separation performance of gas–solid separation fluidized bed with two-size-orifice distributor. Chem. Eng. Res. Des. 168, 397–410, http://dx.doi.org/10.1016/j.cherd.2021.02.008.